

ARTICLE

Open Access

An above-room-temperature phosphonium-based molecular ferroelectric perovskite, $[(\text{CH}_3)_4\text{P}]\text{CdCl}_3$, with Sb^{3+} -doped luminescence

Lin Zhou¹, Ping-Ping Shi¹, Xiao-Ming Liu², Jing-Chun Feng², Qiong Ye¹, Ye-Feng Yao³, Da-Wei Fu¹, Peng-Fei Li¹, Yu-Meng You¹, Yi Zhang¹ and Ren-Gen Xiong¹

Abstract

Molecular ferroelectrics are attracting tremendous interest because of their low cost, mechanical flexibility, easy processing, low weight, and low acoustical impedance. Moreover, their combination of ferroelectric and optical properties has led to investigations of their many potential applications, such as low-energy electron excitation and field emission displays. However, luminescent molecular ferroelectrics have rarely been reported, except for several AMnX_3 -type or lanthanide ion-based luminescent ferroelectrics. Here, we report the first above-room-temperature phosphonium-based molecular ferroelectric perovskite, $[(\text{CH}_3)_4\text{P}]\text{CdCl}_3$ (**1**), with a high Curie temperature ($T_c = 348$ K) and moderate remanent polarization ($P_r = 0.43 \mu\text{C}/\text{cm}^2$). Using piezoresponse force microscopy (PFM), the typical stripe-like domains of ferroelectrics can be observed. Moreover, **1** exhibits orange luminescence under UV excitation after doping with Sb^{3+} , which represents a first step toward realizing luminescence-enhanced molecular ferroelectrics with various wavelengths. These results will inspire the further exploration of phosphonium-based ferroelectrics and pave the way toward practical applications in ferroelectric luminescence and/or multifunctional devices.

Introduction

Ferroelectric materials with luminescent properties are an important class of optoelectronic functional materials that possess great potential for applications in spintronics, photovoltaics, optical–electrical–mechanical actuators, and so on¹. To date, research on luminescent ferroelectrics has mainly focused on inorganic perovskites with a general formula of ABO_3 (where A and B are metal ions with different sizes), which have been widely investigated and found to have numerous applications over the last few

decades^{2,3}. However, due to the pressing environmental and energy issues, their time-consuming, high-cost, and energy-intensive fabrication processes severely hinders the future developments of these inorganic ferroelectrics. Compared with inorganic ABO_3 ferroelectrics, the organic–inorganic hybrid materials in the family of ABX_3 (where A is an organic cation, M is a metal ion, and X is Cl^- , Br^- , I^- , CN^- , HCOO^- or N_3^-) have the advantages of being lightweight, low-cost, and easy to synthesize^{4–6}. Moreover, organic–inorganic hybrid compounds with an ABX_3 perovskite structure are unique candidates for their ability to offer exciting multifunctional properties (including magnetism, electricity, optical, and mechanical)^{7–10}. All of these traits make them promising supplements or alternatives to inorganic ferroelectrics, hence encouraging us to discover new ABX_3 organic–inorganic hybrid luminescent ferroelectrics.


Correspondence: Qiong Ye (yeqiong@seu.edu.cn) or Ye-Feng Yao (yfyao@phy.ecnu.edu.cn) or Ren-Gen Xiong (xiongrg@seu.edu.cn)

¹Ordered Matter Science Research Center, and Jiangsu Key Laboratory for Science and Applications of Molecular Ferroelectrics, Southeast University, 211189 Nanjing, China

²School of Environment and Chemical Engineering, Nanchang Hangkong University, 330063 Nanchang, China

Full list of author information is available at the end of the article.

© The Author(s) 2019

 **Open Access** This article is licensed under a Creative Commons Attribution 4.0 International License, which permits use, sharing, adaptation, distribution and reproduction in any medium or format, as long as you give appropriate credit to the original author(s) and the source, provide a link to the Creative Commons license, and indicate if changes were made. The images or other third party material in this article are included in the article's Creative Commons license, unless indicated otherwise in a credit line to the material. If material is not included in the article's Creative Commons license and your intended use is not permitted by statutory regulation or exceeds the permitted use, you will need to obtain permission directly from the copyright holder. To view a copy of this license, visit <http://creativecommons.org/licenses/by/4.0/>.

Recently, our group reported a series of AMnX_3 -type luminescent ferroelectrics with excellent performances, including (pyrrolidinium) MnCl_3 , (pyrrolidinium) MnBr_3 , (3-pyrrolinium) MnCl_3 , and trimethylchloromethyl ammonium trichloromanganese(II) (TMCM- MnCl_3)^{11–14}. Among them, TMCM- MnCl_3 has shown a large piezoelectric coefficient d_{33} of up to 185 pC/N, which is comparable with that of classical piezoceramics, such as barium titanate (BTO; ~ 190 pC/N)¹¹. Their photoluminescence (PL) can be attributed to the ${}^4\text{T}_1\text{--}{}^6\text{A}_1$ electronic transition of the octahedrally coordinated Mn^{2+} ions, which typically produces a red emission¹⁵. Additionally, several luminescent molecular ferroelectrics based on lanthanide ions have been reported recently^{16–18}. The PL of these materials is intrinsically independent of morphological factors, such as surface defects and crystal sizes; nevertheless, the emission color cannot be tuned because most known luminescent molecular ferroelectrics are Mn-based or lanthanide ion-based.

To date, the A-site organic cation of the ABX_3 molecular ferroelectric family is mostly limited to ammonium cations, and ferroelectrics containing phosphonium cations are very rare. The heavier phosphorus atom and longer P–C bond length may lead to a variety of structures and physical properties. Here, we present a new organic–inorganic hybrid ferroelectric $[(\text{CH}_3)_4\text{P}]\text{CdCl}_3$ (**1**), which has a relatively high Curie temperature ($T_c = 348$ K) and remanent polarization ($P_r = 0.43$ $\mu\text{C}/\text{cm}^2$) compared to those of its isostructural compound $[(\text{CH}_3)_4\text{N}]\text{CdBr}_3$ ¹⁹. To the best of our knowledge, **1** is the first above-room-temperature phosphonium-based molecular ferroelectric with a perovskite structure, which paves the way toward the exploration of phosphonium-based ferroelectrics. Single-crystal structural analysis and solid-state nuclear magnetic resonance (NMR) studies show that the phase transition is associated with an order–disorder transition of the $[(\text{CH}_3)_4\text{P}]^+$ cations. By using piezoresponse force microscopy (PFM), we observed the typically stripe-like domains, which are unprecedented in phosphonium-based ferroelectrics. Additionally, these studies offered direct experimental proof that the switching voltage only needs to be 5 V, which is very favorable to the application of this material in the field of low-power memory. More importantly, after multiple attempts, we found that Sb^{3+} could be successfully introduced into compound **1**, and Sb^{3+} -doped **1** was discovered to emit orange light under UV excitation. Undoubtedly, this work indicates that an increasing number of luminescent ferroelectrics can be rationally designed and constructed rather than being accidentally discovered. Moreover, by introducing different ions, it is possible to introduce emissions of various wavelengths into the ferroelectrics. With these benefits and the excellent ferroelectric properties, **1** shows great potential for application in ferroelectric luminescence and/or multifunctional devices.

Materials and methods

Synthesis

Compound **1** was obtained as colorless prismatic single crystals by the evaporation of an aqueous solution containing stoichiometric amounts of $\text{CdCl}_2 \cdot 2.5\text{H}_2\text{O}$ (4 mmol, 0.9134 g) and tetramethylphosphonium chloride (4 mmol, 0.5062 g) at room temperature. The phase purity of the as-grown crystals was verified by IR and powder X-ray diffraction (PXRD) (Figures S1 and S2). CCDC (The Cambridge Crystallographic Data Centre) 1450378, 1450379, and 1878372 contain the supplementary crystallographic data for this paper. These data can be obtained free of charge from The Cambridge Crystallographic Data Centre via www.ccdc.cam.ac.uk/data_request/cif. The Sb^{3+} -doped variant of **1** was obtained by adding Sb_2O_3 and moderate amounts of HCl (36 wt%, to dissolve Sb_2O_3) to the above mixed solution. The different concentrations of Sb^{3+} in the samples (Sb/Cd molar ratios: 0.03%, 1.2%, and 8.3%) correspond to the initial Sb/Cd molar ratios of 1:40 (Sb_2O_3 : 0.05 mmol, 0.0146 g), 1:20 (Sb_2O_3 : 0.1 mmol, 0.0291 g), and 1:10 (Sb_2O_3 : 0.2 mmol, 0.0583 g) in the solution, respectively.

Methods

The methods used for second harmonic generation (SHG), variable-temperature XRD, dielectric, and polarization-electric field (P – E) hysteresis loop measurements have been described elsewhere¹³. For the dielectric and P – E hysteresis loop measurements, samples were made from single crystals cut into the form of a thin plate perpendicular to the c -axis of the crystal. Silver conductive paste was deposited on the plate surfaces, which were used as the electrodes.

Differential scanning calorimetry (DSC) and PXRD measurements

DSC measurements were performed on a Netzsch DSC 200 F3 instrument under a nitrogen atmosphere in aluminum crucibles with a heating or cooling rate of 10 K/min. PXRD data were measured on a PANalytical X'Pert PRO X-ray diffractometer at room temperature. Diffraction patterns were collected in the range of $2\theta = 5\text{--}50^\circ$ with a step size of 0.02° .

Solid-state NMR measurements

The high-resolution solid-state ${}^{31}\text{P}$ MAS NMR spectra were measured on a Bruker AVANCE III 600 spectrometer operating at 243.94 MHz for detection of ${}^{31}\text{P}$. A 4 mm double resonance MAS probe was used for the experiments. The spinning speed was 6 kHz. The 90° pulse length was 4.0 μs , and the recycle delay was set to 4 s. The ${}^{31}\text{P}$ chemical shifts were calibrated using 1 M H_3PO_4 as the reference ($\delta = 0$ ppm).

PFM measurement

PFM visualization of the ferroelectric domain structures was carried out using a commercial atomic force microscopy system (MFP-3D, Asylum Research). Conductive Pt/Ir-coated silicon probes (EFM, Nanoworld) were used for domain imaging and polarization switching studies. The resonant-enhanced PFM mode was used to enhance the signal, with a typical AC voltage frequency of ~ 320 kHz and an AC amplitude of 2.0 V. Thin films of **1** were used for the PFM measurement. To fabricate thin films of **1**, a precursor solution was obtained by dissolving powder of **1** in deionized water at a concentration of 100 mg/mL. A drop (20 μL) of the precursor solution was carefully spread onto the surface of indium tin oxide (ITO)-coated glass. After annealing the film-coated substrate on a hotplate at 323 K for 20 min, a thin film of **1** had grown in situ on the substrate.

Elemental analysis and PL measurement

All elemental ratios were determined by a SPECTRO-BLUE ICP-OES. The emission spectra were measured at room temperature on a Hitachi Model F-7000 FL spectrophotometer equipped with a 150 W xenon lamp and electron beam as the excitation source.

Results and discussion

High-quality large single crystals of **1** were obtained from an aqueous solution in high yield. Then, to detect the phase transition behavior, DSC measurements were performed on powder samples of **1** over the temperature range of 280–400 K. The DSC curves reveal that **1** undergoes a reversible phase transition near $T_c = 348$ K, where a pair of endothermic and exothermic peaks appear (Fig. 1). Both the narrow thermal hysteresis of 4 K and the broad peak shape of the heating curves suggest that the phase transition should be a second-order transition²⁰.

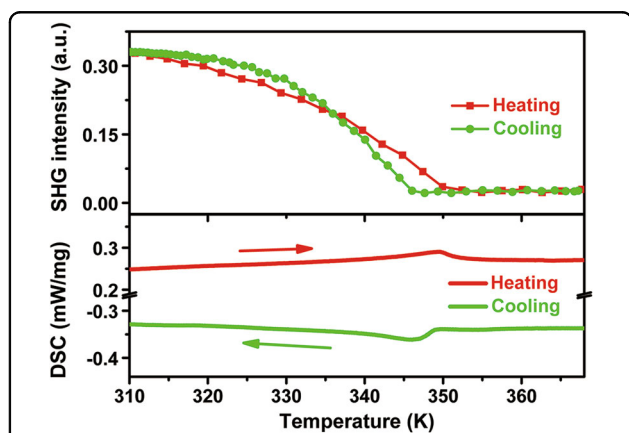
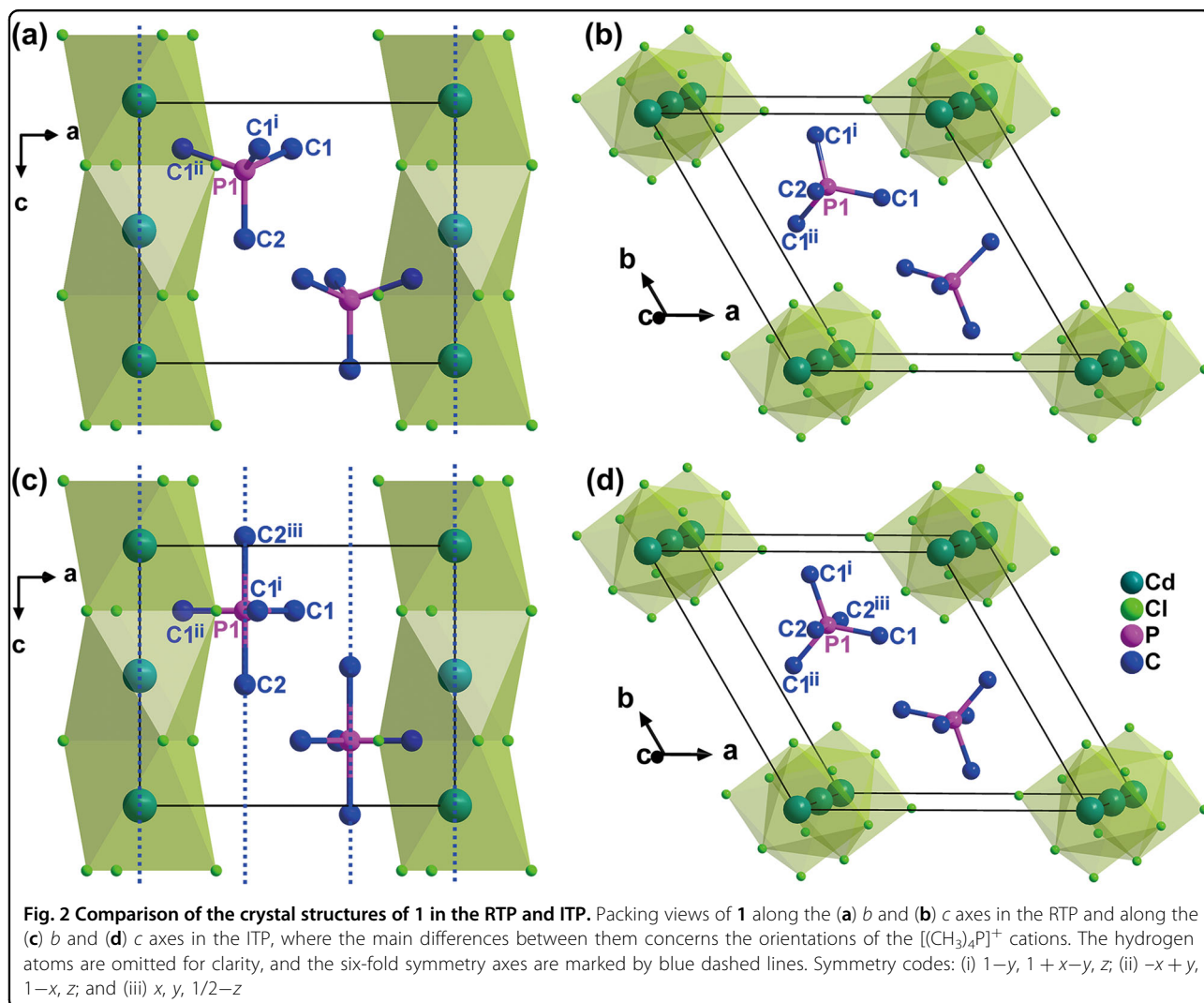


Fig. 1 Thermal and SHG properties of **1**. DSC curves (bottom) and temperature-dependent SHG intensity (top) for **1**, which reveal a reversible structural phase transition near 348 K

A second inconspicuous second-order phase transition was found near $T_2 = 387$ K, as shown in Figure S3.

Taking into account the DSC results, determination of the crystal structures is particularly necessary for understanding the phase transition mechanism. At 293, 373, and 393 K, corresponding to the room-temperature phase (RTP), intermediate-temperature phase (ITP), and high-temperature phase (HTP), respectively, **1** was first considered to crystallize into the centrosymmetric hexagonal space group $P6_3/m$ (point group $6/m$), as depicted by the XRD analysis and PLATON program. However, the presence of a pseudocenter of symmetry makes the crystal symmetry difficult to accurately determine²¹. From the XRD analysis, the RTP can also be solved in the polar space group $P6_3$, which has an active second-harmonic generation (SHG) effect. However, the SHG effect vanishes in the centrosymmetric point group $P6_3/m$. Therefore, the SHG measurement is a useful method to confirm the space group and detect the structural changes that occur during the phase transition. As shown in Fig. 1 and Figure S3, for **1**, the SHG intensity has an active value below 348 K, indicating a noncentrosymmetric crystal structure in the RTP, whereas above 348 K, the vanishing SHG signal is in good agreement with a centrosymmetric ITP and HTP. Moreover, the continuous decrease of the SHG intensity in the vicinity of T_c is characteristic of a second-order phase transition as found in the DSC result. Based on these results, the RTP of **1** was finally defined as the polar hexagonal space group $P6_3$ (point group 6) (Table S2). With a decrease of symmetry elements from 12 ($E, 2C_6, 2C_3, C_2, i, 2S_3, 2S_6, \sigma_h$) in the ITP to 6 ($E, 2C_6, 2C_3, C_2$) in the RTP, the symmetry-breaking from $P6_3/m$ to $P6_3$ is described by the Aizu notation of $6/mF6$, belonging to one of the 88 paraelectric-to-ferroelectric phase transitions²¹. Particularly, in view of the Landau phase transition theory, such halving of the symmetry elements is typical of a second-order ferroelectric phase transition, which is distinctly different from that occurring in the low-temperature ferroelectric $[(\text{CH}_3)_4\text{N}]\text{CdBr}_3$, which demonstrates symmetry breaking from $P6_3/m$ to $P6_1$ at 156 K¹⁹.

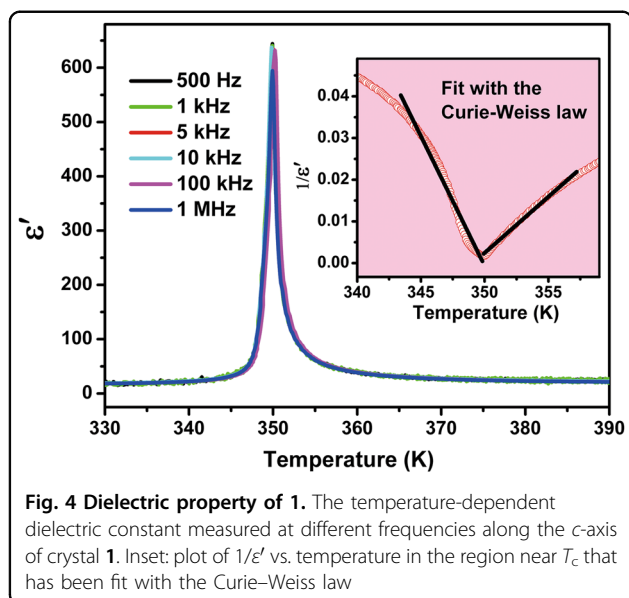
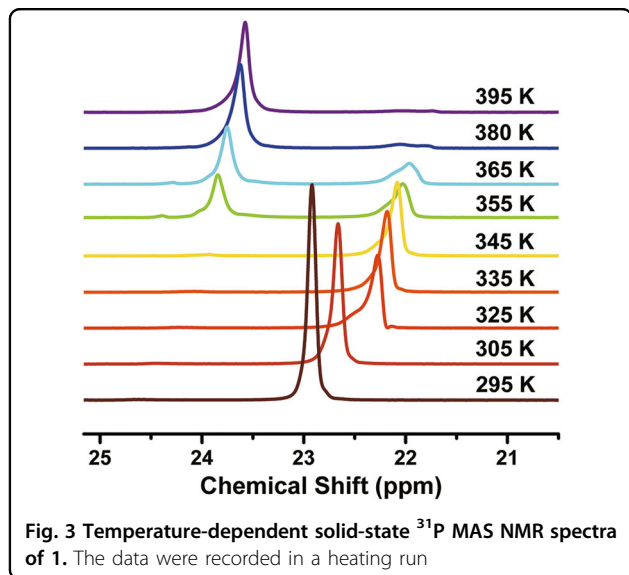
In RTP, ITP, and HTP, the coordination geometry of the Cd center can be described as a slightly distorted octahedron fulfilled by six Cl atoms, while the $[\text{CdCl}_3]^-$ chains are connected by these face-sharing $[\text{CdCl}_6]$ octahedrons (Fig. 2). Within the inorganic anionic chains of the three phases, the Cd centers are all located at the six-fold symmetry axes (Figure S4). As the phase transition between the ITP and HTP is an isostructural one (both $P6_3/m$, see Table S2), we will not discuss their structural changes in detail. Triggered by the temperature change, the geometries of the $[\text{CdCl}_6]$ octahedrons show only slight differences between the RTP and ITP (Tables S3 and S4). The Cd—Cl bond distances in the RTP range



from 2.6435(17) to 2.6573(17) Å, while those in the ITP are 2.6515(5) Å. Correspondingly, the Cl—Cd—Cl bond angles also change from 84.03(6)°, 83.50(6)°, and 96.236(15)° in the RTP to 83.570(15)° and 96.430(15)° in the ITP, with the Cd—Cl—Cd bond angle varying from 79.14(2)° to 79.40(2)°. In contrast to the minor positional changes of the Cl atoms, the shift in the $[(\text{CH}_3)_4\text{P}]^+$ cations is more remarkable. In the RTP, the $[(\text{CH}_3)_4\text{P}]^+$ cations are ordered with the P1—C2 bonds lying on the three-fold symmetry axis, and all the P—C bond distances and C—P—C bond angles are comparable to those found in other phosphonium compounds^{22,23}. When the temperature increases, the $[(\text{CH}_3)_4\text{P}]^+$ cations are converted to a disordered state in the ITP, where the P1 and C1 atoms occupy the mirror plane perpendicular to the six-fold symmetry axes and the P1—C2 bonds are located on the six-fold symmetry axis to satisfy the higher crystal symmetry. In addition to

the special conformation and abnormal geometric parameters, the large thermal ellipsoids of the $[(\text{CH}_3)_4\text{P}]^+$ cations, depicted in Figure S5, further verify the molecular disorder. Therefore, the order–disorder transition of the $[(\text{CH}_3)_4\text{P}]^+$ cations might give rise to the structural phase transition and the ferroelectricity along the *c*-axis.

To gain deeper insight into the local structure of the $[(\text{CH}_3)_4\text{P}]^+$ cations, we measured the variable-temperature ^{31}P MAS NMR spectra for **1** within 295–395 K (Fig. 3). At 295 K, an obvious peak can be observed at 22.92 ppm, indicating that only one type of phosphorus environment exists in the RTP. With increasing temperature, the chemical shift shows a clear high-field shift, which can most likely be attributed to a variation in the phosphine environment arising from lattice expansion. When the temperature reaches 355 K, two main peaks at 22.03 and 23.84 ppm emerge, indicating the presence of the different phosphonium cations in ITP^{24,25}.



The origin of the different phosphonium cations is related to the two conformations in the ITP. This is in agreement with the crystal structure analysis, where the electron cloud of the phosphonium cations shows different shapes, indicating the presence of different conformations for the phosphonium cations. As the temperature continues to rise, the peak near 22 ppm decreases until nearly vanishing at 395 K. This can be attributed to the fast isotropic motion of the $[(\text{CH}_3)_4\text{P}]^+$ cations in the HTP, which are allowed by the larger crystal lattice of this phase. This is also in agreement with the observations of the crystal structure analysis, which show that the electron cloud of the $[(\text{CH}_3)_4\text{P}]^+$ cations becomes uniform in the HTP (see Figure S5). The ^{31}P MAS NMR observations herein

provide clear proof for the order–disorder transition of the $[(\text{CH}_3)_4\text{P}]^+$ cations in **1** near T_c .

For ferroelectrics, a significant change in the dielectric constant near T_c is well known to be a direct sign of a proper paraelectric-to-ferroelectric phase transition, that is, the so-called λ -type dielectric change. Thus, the temperature-dependent complex dielectric constants ($\epsilon = \epsilon' - i\epsilon''$, where ϵ' and ϵ'' are the real and imaginary parts, respectively) were measured in the frequency range of 500 Hz to 1 MHz along the crystal *c*-axis of **1**, as illustrated in Fig. 4. The frequency-independent nature of ϵ' in the measured temperature range signifies that the orientations of the dipolar moments easily follow the oscillating electric field. Compared with the insignificant 20% change and improper nature of the ϵ' of $[(\text{CH}_3)_4\text{N}]\text{CdBr}_3$ ¹⁹, for **1**, a prominent peak-like dielectric change appears near T_c , where ϵ' undergoes a 30-fold increase, is definitive evidence of a proper ferroelectric phase transition. Additionally, in the vicinity of T_c , ϵ' shows Curie–Weiss behavior, i.e., $\epsilon' = C_{\text{para}}/(T - T_0)$, where ($T > T_c$) or $C_{\text{ferro}}/(T_0' - T)$ where ($T < T_c$), where C_{para} and C_{ferro} are the Curie–Weiss constants of the ITP and RTP, respectively. The Curie–Weiss constants obtained from fitting (Table S1) fall within the order of 10^2 K, lower than those of typical displacive (10^5 K) and order–disorder-type (10^3 K) ferroelectrics but comparable to those found in colemanite, NH_4HSO_4 , $(\text{CH}_3\text{NH}_3)\text{Al}(\text{SO}_4)_2 \cdot 12\text{H}_2\text{O}$, and $[\text{NH}_2\text{CH}_2\text{COOH}]_2\text{HNO}_3$ ^{26,27}. In the case of **1**, C_{para} and C_{ferro} at 1 MHz are estimated to be 366 and 161 K, respectively, and the Curie–Weiss temperatures ($T_0 \approx T_0' = 350$ K) are almost equal to T_c . The $C_{\text{para}}/C_{\text{ferro}}$ ratio of 2.27 at 1 MHz is smaller than 4, which is indicative of a second-order ferroelectric phase transition.

Despite the above-described symmetry breaking, Curie temperature, and notable dielectric changes, the identification of ferroelectricity in **1** should rely on the observation of *P*–*E* hysteresis loops, as polarization switching is the most common characteristic of ferroelectrics. At 323 K, typical *P*–*E* hysteresis loops can be obtained with a capacitor configuration sandwiched by a pair of Ag electrodes at 200, 100, 50, and 20 Hz (Fig. 5). The observed remanent polarization (P_r) and coercive field (E_c) are $\sim 0.43 \mu\text{C}/\text{cm}^2$ and 3.4 kV/cm at 20 Hz, respectively. With increasing frequency, the P_r has almost no change, and the E_c increases within the measured frequency range. Comparing the *P*–*E* hysteresis loops measured at 311 and 323 K, a decrease in both the P_r and E_c can be found at the higher temperature (Figure S6). This may be attributed to the disrupted long-range order of the polarization and the weakened coupling stabilizing effect between the charged defects and domains that are caused by an increase in thermal fluctuations²⁸. Consequently, **1** has been demonstrated as a molecular ferroelectric compound, in which P_r is significantly larger than that of its analog,

$[(\text{CH}_3)_4\text{N}]\text{CdBr}_3$, which has a P_r of $0.010 \mu\text{C}/\text{cm}^2$ ¹⁹. Additionally, based on the crystal structures of **1** and $[(\text{CH}_3)_4\text{N}]\text{CdBr}_3$ in their ferroelectric phases²⁹, we assume

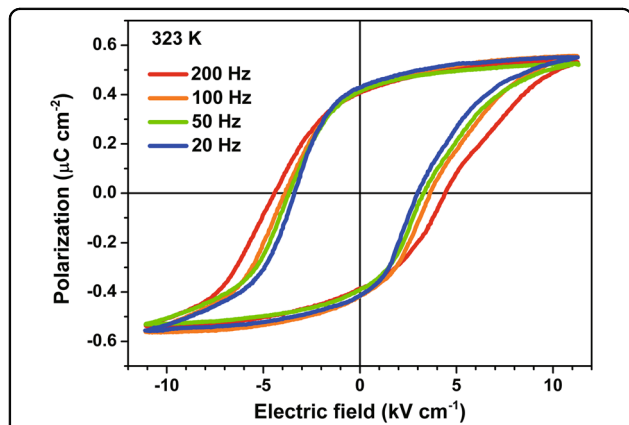


Fig. 5 Polarization reversal of 1. Electric polarization (P) vs. electric field (E) hysteresis loops along the $[001]$ -direction of **1** measured at different frequencies by a typical Sawyer–Tower circuit at 323 K

that the positive charges and the negative charges in the unit cell are on the P/N and Cd atoms, respectively (Figures S12 and S13). Then, the greater shift in **1** between its positive and negative charges is calculated to induce a higher polarization of $\sim 0.72 \mu\text{C}/\text{cm}^2$ for **1**, compared with $0.13 \mu\text{C}/\text{cm}^2$ for $[(\text{CH}_3)_4\text{N}]\text{CdBr}_3$ (see Supplementary Information), both of which are higher than their experimental values.

By imaging and manipulating the polarization vector or ferroelectric domain at the nanoscale, the PFM technique has opened the way to explore microscopic ferroelectricity, whose macroscopic manifestations are determined by the P – E hysteresis loops^{30,31}. Fig. 6a–c and S7 present the PFM phase and amplitude images and the topographic image of the crystal surface of **1**, acquired over an area of $6 \mu\text{m} \times 6 \mu\text{m}$. The phase signal represents the polarization direction, and the amplitude signal is proportional to the reciprocal piezoelectric constant. Each PFM image includes two components: (i) a vertical PFM image, determined by recording the tip deflection signal at the frequency of modulation and (ii) a lateral PFM image, measured as the

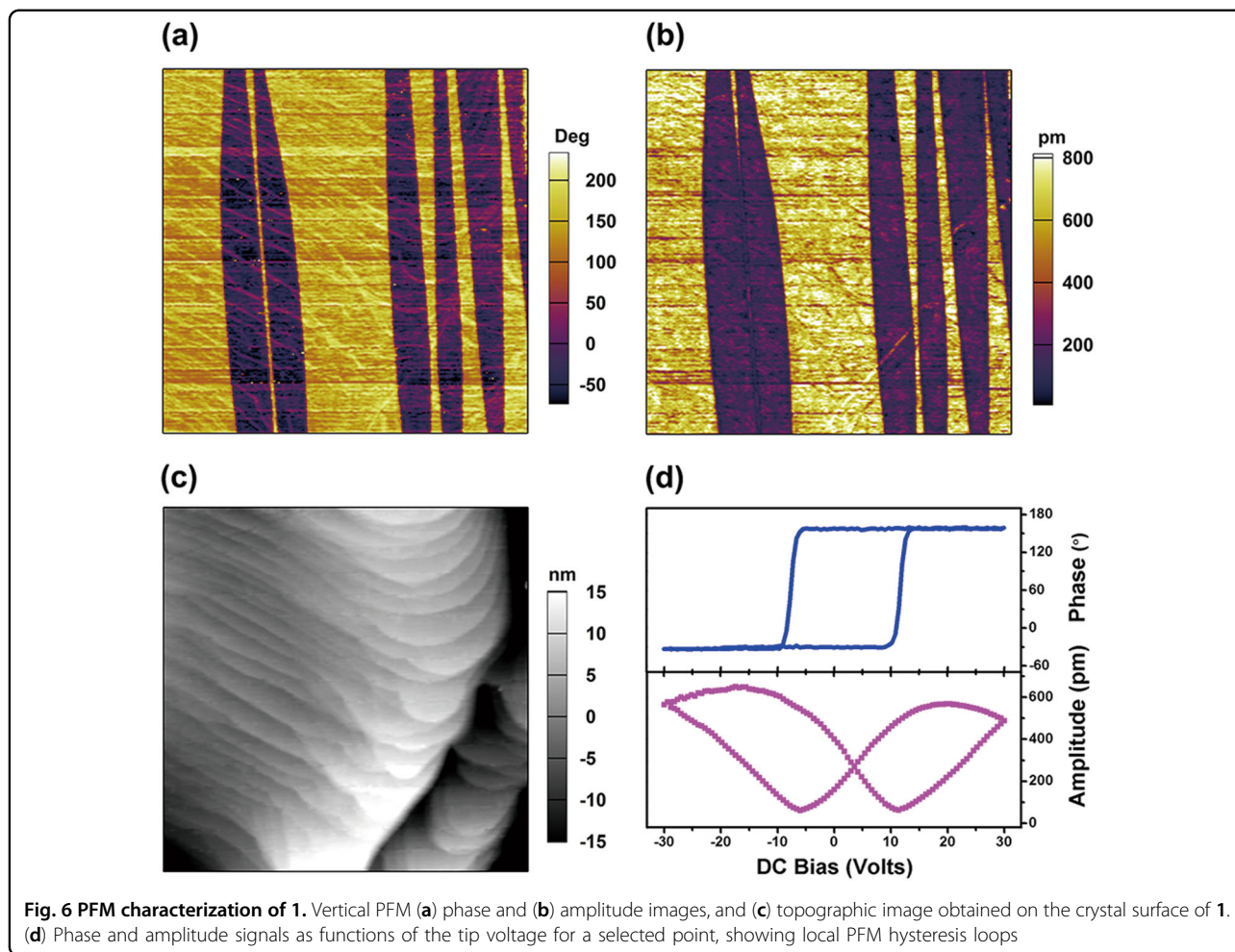
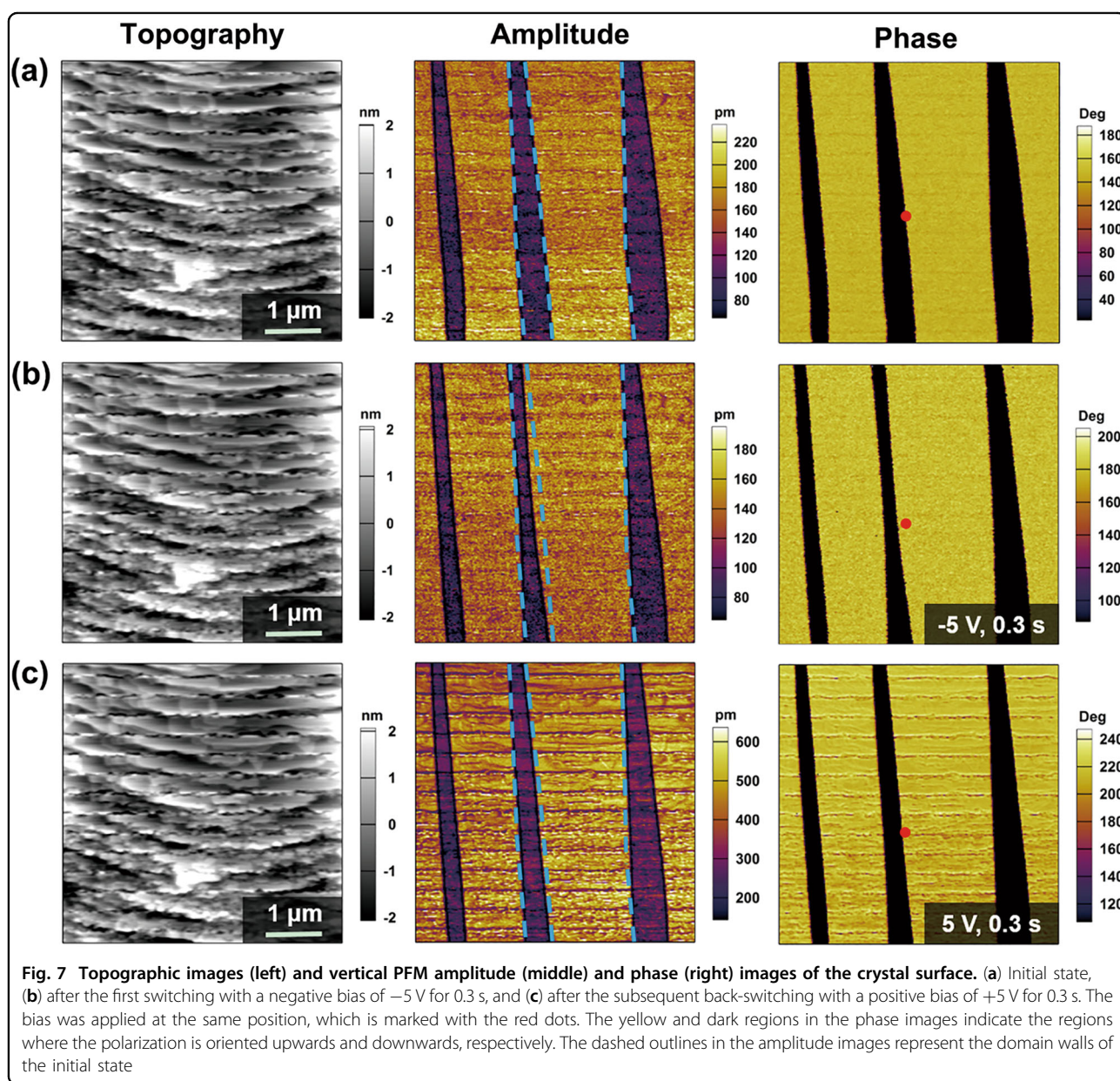


Fig. 6 PFM characterization of 1. Vertical PFM (a) phase and (b) amplitude images, and (c) topographic image obtained on the crystal surface of **1**. (d) Phase and amplitude signals as functions of the tip voltage for a selected point, showing local PFM hysteresis loops

lateral motion of the cantilever owing to bias-induced surface shearing^{32,33}. It is notable that the two images of this surface region reveal the same domain distributions, with typical stripe-like domain structures. The amplitude image shows two antiparallel domains with clear contrast, separated by the domain walls (Fig. 6b), which coincide with the regions of significant contrast in the phase image (Fig. 6a). Figure 6d depicts the local PFM responses at a point on the crystal surface, demonstrating the characteristic hysteretic behaviors of the phase and amplitude signals, which are typical for the switching of ferroelectric domains. To further visualize the polarization switching, we scanned the initial as-grown state over an area of $5\ \mu\text{m} \times 5\ \mu\text{m}$ (Fig. 7a), in

which the position marked with a red dot was point poled for 0.3 s with a tip bias of $-5\ \text{V}$. In the phase image, the domain indicated by the dark color distinctly shrank, whereas the bright-colored domain expanded, suggesting a switching of the polarization state (Fig. 7b). Then, by subsequent poling for 0.3 s with an opposing tip bias of $+5\ \text{V}$, the polarizations of the domains switched back, as shown in Fig. 7c. These observations reveal that the domains in **1** are switchable under an external field, further confirming the material is ferroelectric.

Both the excellent ferroelectric performance and the high tunability of the organic–inorganic hybrid structure motivated us to investigate the potential multifunctionality of **1**.



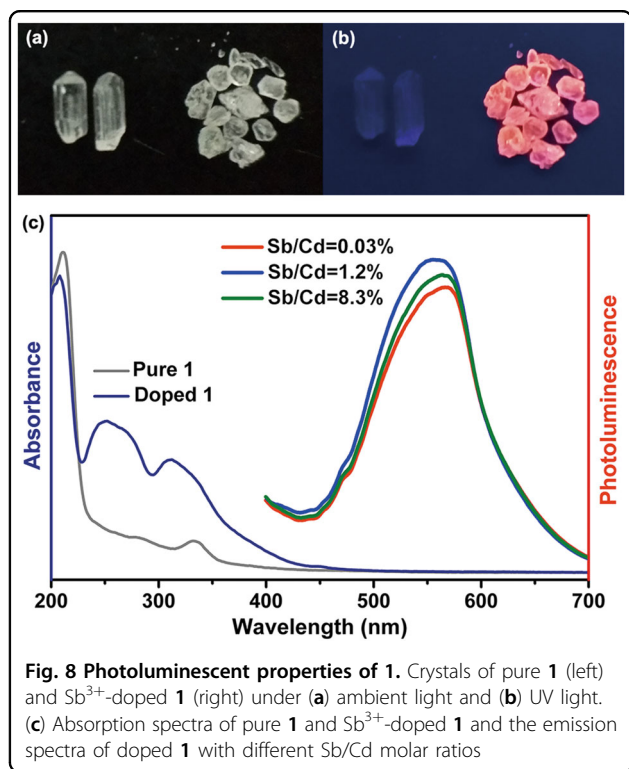


Fig. 8 Photoluminescent properties of **1**. Crystals of pure **1** (left) and Sb^{3+} -doped **1** (right) under (a) ambient light and (b) UV light. (c) Absorption spectra of pure **1** and Sb^{3+} -doped **1** and the emission spectra of doped **1** with different Sb/Cd molar ratios

Amazingly, the successful doping of Sb^{3+} into **1** was first evidenced by observing its orange emission under excitation with a UV lamp. By varying the Sb/Cd molar ratio in solution, different concentrations of Sb^{3+} can be achieved in the samples. The actual concentrations of Sb^{3+} were determined by ICP-OES elemental analysis, and the Sb^{3+} concentrations in the samples are always lower than those added to the reaction mixtures. Figure S8 shows the PXRD patterns for the pure and Sb^{3+} -doped samples of **1** at room temperature, where the molar ratios of Sb/Cd are 0%, 0.03%, 1.2%, and 8.3%. There is no obvious difference between the PXRD patterns of the pure sample and the samples doped with various Sb^{3+} concentrations, indicating that the hexagonal polar structure is preserved after Sb-doping. The ferroelectricity of the Sb^{3+} -doped samples of **1** was confirmed by their P - E hysteresis loops and PFM measurements (Figures S9 and S10).

As a primary or sensitizing activator, the $5s^2 \text{Sb}^{3+}$ ion has been widely used in phosphors, such as calcium halophosphate codoped with Sb^{3+} and Mn^{2+} , which is an important commercial phosphor³⁴. In general, the luminescence properties of s^2 ions are susceptible to influence from the host lattice^{35,36}. From Fig. 8a, b, we can see that pure **1** is not photoluminescent under either ambient light or the UV lamp. However, the Sb^{3+} -doped crystals of **1** that are colorless under ambient light emit intense orange light when exposed to a UV lamp. Undoubtedly, their PL arises from the addition of Sb^{3+} . The absorption spectra

of pure **1** and doped **1** consist of several bands in the UV region and are quite different, as shown in Fig. 8c. By exciting Sb^{3+} -doped **1** with 320 nm light at room temperature, the PL spectra present one broad emission band in the visible region centered near 563 nm. As the concentration of Sb^{3+} increases, the PL intensity has little variation, and the maximum of the band shifts slightly. The photoluminescence excitation (PLE) spectra for ~563 nm emission show similar bands as the absorption spectrum of doped **1** (Figure S11). In future studies, we expect to find additional dopants that can be used to tune the emission of **1**.

Conclusion

In summary, $[(\text{CH}_3)_4\text{P}]\text{CdCl}_3$ is a unique molecular ferroelectric compound combining high-temperature ferroelectricity and Sb^{3+} -doped luminescence and is an ideal candidate for application in multifunctional ferroelectric devices. Compared with $[(\text{CH}_3)_4\text{N}]\text{CdBr}_3$, the introduction of a phosphonium cation not only modifies the organic-inorganic hybrid structure but also successfully improves the T_c , dielectric response, and P_r . More significantly, the doping of Sb^{3+} into the crystal structure results in intriguing photoluminescent properties. The exploration of phosphonium-based systems by a doping strategy will open new avenues to design an increasing number of multifunctional luminescent molecular ferroelectric compounds for potential applications in spintronics, photovoltaics, optical-electrical-mechanical actuators, etc.

Acknowledgements

This work was financially supported by the National Natural Science Foundation of China (21471032, 21771037, and 21805033), the Natural Science Foundation of Jiangsu Province (JNSF) (BK20170659) and Shanghai Key Laboratory of Magnetic Resonance Open Project Funding.

Author details

¹Ordered Matter Science Research Center, and Jiangsu Key Laboratory for Science and Applications of Molecular Ferroelectrics, Southeast University, 211189 Nanjing, China. ²School of Environment and Chemical Engineering, Nanchang Hangkong University, 330063 Nanchang, China. ³Physics Department & Shanghai Key Laboratory of Magnetic Resonance, School of Physics and Materials Science, East China Normal University, North Zhongshan Road 3663, 200062 Shanghai, China

Conflict of interest

The authors declare that they have no conflict of interest.

Publisher's note

Springer Nature remains neutral with regard to jurisdictional claims in published maps and institutional affiliations.

Supplementary information is available for this paper at <https://doi.org/10.1038/s41427-019-0115-0>.

Received: 26 April 2018 Revised: 12 November 2018 Accepted: 31 December 2018.

Published online: 5 April 2019

References

1. Yamamoto, H., Okamoto, S. & Kobayashi, H. Luminescence of rare-earth ions in perovskite-type oxides: from basic research to applications. *J. Lumin.* **100**, 325–332 (2002).
2. Hao, J., Zhang, Y. & Wei, X. Electric-induced enhancement and modulation of upconversion photoluminescence in epitaxial BaTiO₃: Yb/Er thin films. *Angew. Chem.* **123**, 7008–7012 (2011).
3. Sun, Q. et al. Effects of temperature and electric field on upconversion luminescence in Er³⁺-Yb³⁺ codoped Ba_{0.8}Sr_{0.2}TiO₃ ferroelectric ceramics. *J. Am. Ceram. Soc.* **100**, 4661–4669 (2017).
4. Shi, C., Zhang, X., Cai, Y., Yao, Y.-F. & Zhang, W. A chemically triggered and thermally switched dielectric constant transition in a metal cyanide based crystal. *Angew. Chem. Int. Ed.* **54**, 6206–6210 (2015).
5. Du, Z.-Y. et al. Switchable guest molecular dynamics in a perovskite-like coordination polymer toward sensitive thermoresponsive dielectric materials. *Angew. Chem. Int. Ed.* **54**, 914–918 (2015).
6. Chen, S., Shang, R., Wang, B.-W., Wang, Z.-M. & Gao, S. An A-site mixed-ammonium solid solution perovskite series of [(NH₂NH₃)_x(CH₃NH₃)_{1-x}][Mn(HCOO)₃] (x=1.00-0.67). *Angew. Chem. Int. Ed.* **54**, 11093–11096 (2015).
7. Tian, Y. et al. Observation of resonant quantum magnetoelectric effect in a multiferroic metal-organic framework. *J. Am. Chem. Soc.* **138**, 782–785 (2016).
8. Yamada, K. et al. Phase transition and electric conductivity of A_nSnCl₃ (A=Cs and CH₃NH₂). *Bull. Chem. Soc. Jpn.* **71**, 127–134 (1998).
9. Sun, Z. et al. A photoferroelectric perovskite-type organometallic halide with exceptional anisotropy of bulk photovoltaic effects. *Angew. Chem. Int. Ed.* **55**, 6545–6550 (2016).
10. Shang, R., Wang, Z.-M. & Gao, S. A 36-fold multiple unit cell and switchable anisotropic dielectric responses in an ammonium magnesium formate framework. *Angew. Chem. Int. Ed.* **54**, 2534–2537 (2015).
11. You, Y.-M. et al. An organic-inorganic perovskite ferroelectric with large piezoelectric response. *Science* **357**, 306–309 (2017).
12. Ye, H.-Y. et al. High-temperature ferroelectricity and photoluminescence in a hybrid organic-inorganic compound(3-pyrrolinium) MnCl₃. *J. Am. Chem. Soc.* **137**, 13148–13154 (2015).
13. Zhang, Y. et al. Highly efficient red-light emission in an organic-inorganic hybrid ferroelectric: (pyrrolidinium)MnCl₃. *J. Am. Chem. Soc.* **137**, 4928–4931 (2015).
14. Zhang, Y. et al. The first organic-inorganic hybrid luminescent multiferroic: (pyrrolidinium)MnBr₃. *Adv. Mater.* **27**, 3942–3946 (2015).
15. Blasse, G. & Grabmaier, B. C. *Luminescent Materials*, 1st edn (Springer-Verlag, Berlin Heidelberg, 1994).
16. Guo, P.-H. et al. A zigzag Dy^{III}4 cluster exhibiting single-molecule magnet, ferroelectric and white-light emitting properties. *J. Mater. Chem. C* **2**, 8858–8864 (2014).
17. Guo, P.-H. et al. Multifunctional Dy^{III}4 cluster exhibiting white-emitting, ferroelectric and single-molecule magnet behavior. *Chem.-Eur. J.* **19**, 8769–8773 (2013).
18. Long, J. et al. A high-temperature molecular ferroelectric Zn/Dy complex exhibiting single-ion-magnet behavior and lanthanide luminescence. *Angew. Chem. Int. Ed.* **54**, 2236–2240 (2015).
19. Gesi, K. Ferroelectricity in N(CH₃)₄CdBr₃. *J. Phys. Soc. Jpn.* **59**, 432–434 (1990).
20. Li, L. et al. Tailored engineering of an unusual (C₄H₉NH₃)₂(CH₃NH₃)₂Pb₃Br₁₀ two-dimensional multilayered perovskite ferroelectric for a high-performance photodetector. *Angew. Chem.* **129**, 12318–12322 (2017).
21. Shi, P.-P. et al. Symmetry breaking in molecular ferroelectrics. *Chem. Soc. Rev.* **45**, 3811–3827 (2016).
22. Jin, L. et al. Structure and transport properties of a plastic crystal ion conductor: diethyl(methyl)(isobutyl)phosphonium hexafluorophosphate. *J. Am. Chem. Soc.* **134**, 9688–9697 (2012).
23. Shi, P.-P. et al. Novel phase-transition materials coupled with switchable dielectric, magnetic, and optical properties: [(CH₃)₄P][FeCl₄] and [(CH₃)₄P][FeBr₄]. *Chem. Mater.* **26**, 6042–6049 (2014).
24. Akutagawa, T. et al. Ferroelectricity and polarity control in solid-state flip-flop supramolecular rotators. *Nat. Mater.* **8**, 342–347 (2009).
25. Shao, X.-D., Zhang, X., Shi, C., Yao, Y.-F. & Zhang, W. Switching dielectric constant near room temperature in a molecular crystal. *Adv. Sci.* **2**, 1500029 (2015).
26. Nakamura, E., Mitsui, T. & Furuichi, J. A note on the classification of ferroelectrics. *J. Phys. Soc. Jpn.* **18**, 1477–1481 (1963).
27. Draeger, D. & Singh, S. Dielectric susceptibility and the order of ferroelectric phase transitions. *Solid State Commun.* **9**, 595–597 (1971).
28. Jin, L., Li, F. & Zhang, S. Decoding the fingerprint of ferroelectric loops: comprehension of the material properties and structures. *J. Am. Ceram. Soc.* **97**, 1–27 (2014).
29. Aguirrezamalloa, G., Madariaga, G., Couzi, M. & Breczewski, T. X-ray diffraction study of the ferroelectric phase transition of (CH₃)₄NCdBr₃ (TMCB). *Acta Crystallogr. Sect. B* **49**, 691–698 (1993).
30. Kalinin, S. V. et al. Ferroelectric lithography of multicomponent nanostructures. *Adv. Mater.* **16**, 795–799 (2004).
31. Tang, Y.-Y. et al. Visualization of room-temperature ferroelectricity and polarization rotation in the thin film of quinuclidinium perchlenate. *Phys. Rev. Lett.* **119**, 207602 (2017).
32. Tang, Y.-Y. et al. A multiaxial molecular ferroelectric with highest Curie temperature and fastest polarization switching. *J. Am. Chem. Soc.* **139**, 13903–13908 (2017).
33. Lu, H. et al. Statics and dynamics of ferroelectric domains in diisopropylammonium bromide. *Adv. Mater.* **27**, 7832–7838 (2015).
34. Yen, W. M., Shionoya, S. & Yamamoto, H. *Phosphor Handbook*, 2nd edn (CRC Press, Boca Raton, FL, USA, 2006).
35. Yamashita, N., Sasaki, Y.-i & Nakamura, K. Photoluminescence of Sb³⁺ centers in SrS and SrSe. *Jpn. J. Appl. Phys.* **31**, 2791–2797 (1992).
36. Oomen, E., Peeters, R., Smit, W. & Blasse, G. The luminescence of the Sb³⁺ ion in Ln(PO₃)₃ (Ln=Sc, Lu, Y, Gd, La). *J. Solid State Chem.* **73**, 151–159 (1988).